Frontiers of Materials Science

**Electronic Supplementary Material**

# Titanium carbide-functionalized cobalt selenide as a heterogeneous electro-Fenton cathode catalyst for the degradation of sulfamerazine

Chunhui Yu, Kuobo Wang, Yingtao Fan, Fan Yang (✉), Kexin Wei, Chenlin Wang, Xinyang Sun, Junpu An, Xiao Zhang (✉), and Yongfeng Li (✉)

State Key Laboratory of Heavy Oil Processing, China University of Petroleum, Beijing 102249, China

E-mails: yangfan@cup.edu.cn (F.Y.), zhangxiao@cup.edu.cn (X.Z.), yfli@cup.edu.cn (Y.L.)

## 1 Chemicals and reagents

Chemicals and reagents used in this work, including cobalt sulfate heptahydrate ($CoSO_4·7H_2O$, 99%), hydrazine hydrate ($N_2H_4·H_2O$, analytical reagent (AR)), sodium selenite ($Na_2SeO_3$, ≥ 90%), titanium-carbide aluminum ($Ti_3AlC_2$, 98%), lithium fluoride (LiF, 99%), hydrochloric acid (HCl, ≥ 37% ), sulfamerazine (SMR, 99%), anhydrous sodium sulfate ($Na_2SO_4$, 99%), formic acid ($CH_2O_2$, ≥ 96%), acetonitrile ($C_2H_3N$, ≥ 99.9%), concentrated sulfuric acid ($H_2SO_4$, 98%), phosphoric acid ($H_3PO_4$, 85%), sodium hydroxide (NaOH, 96%), florfenicol (FLO, 99%), ciprofloxacin (CIP, 99%), bisphenol A (BPA, 99%), sodium bicarbonate ($NaHCO_3$, ≥ 99.8%), sodium chloride (NaCl, 99.5%), dibasic sodium phosphate ($Na_2HPO_4$, 99.9%), sodium nitrate ($NaNO_3$, ≥ 98.5%), tert-butanol (TBA, 99.5%), p-benzoquinone (BQ, 97%), and L-histamine (L-H, ≥ 99%), catalase (CAT, ≥ 200 000 units/g), 5,5-dimethylpyrroline-1-oxide (DMPO, ≥ 97%), and 2,2,6,6-tetramethylpiperidine (TEMP, 99%), were purchased from Beijing InnoChem Science & Technology Co., Ltd., China.

## 2 Materials characterization

To test the morphology of prepared samples, scanning electron microscopy (SEM) and transmission electron microscopy (TEM) were carried out using a Hitachi SU8010 instrument (Japan) and a Tecnai G2 F20 instrument (FEI, USA), respectively. The crystal structures of all samples were determined through X-ray diffraction (XRD) using an diffractometer (Bruker D8 Advance, Germany) at a scanning rate of $2(°)·min^{-1}$. The chemical states of samples were characterized through X-ray photoelectron spectroscopy (XPS) using an instrument (Thermo Fisher K-alpha) with an Al-Kα X-ray source. The leached amounts of Co were tested using an ion chromatograph (Thermo Scientific ICS-5000+). Reactive oxygen species (ROS) including •OH, $•O_2^-$, and $^1O_2$ were captured using TEMP and DMPO as spin collectors, and the free radical signals were measured via electron paramagnetic resonance (EPR) using a spectrometer (Bruker EMXnano, Germany).

## 3 Electrochemical measurements

All electrochemical tests were performed at the CHI760E Electrochemical Workstation (CHI Instruments Inc. Shanghai, China) at room temperature with an electrolyte of 0.1 mol·L$^{-1}$ $Na_2SO_4$ solution. The counter electrode, the working electrode, and the reference electrode were a platinum sheet electrode (1 cm × 1 cm), a prepared cathode, and an Ag/AgCl electrode, respectively. The conversion potential of $E$(RHE) was determined according to Eq. (1) as follows:

$$E(\mathrm{RHE}) = E(\mathrm{Ag/AgCl}) + 0.059 \times \mathrm{pH} + 0.197 \quad \text{(S1)}$$

Electrochemical impedance spectroscopy (EIS) was used to measure the charge transfer resistance of the samples in the frequency range of 0.01–$10^6$ Hz. Double-layer capacitance ($C_{dl}$) values were employed to estimate the electrochemical surface areas (ECSAs) of samples, which were calculated base on the cyclic voltammetry (CV) results in the non-Faradaic potential region ranging from −0.1 to 0.1 V *vs.* RHE at 50, 100, 150, 200 and 250 mV·s$^{-1}$.

ORR properties of materials were tested using a three-electrode system with the rotating disk electrode (RDE; Pine, USA). The test was carried out in the 0.1 mol·L$^{-1}$ $Na_2SO_4$ solution, the disk electrode area was 0.2475 cm$^{-2}$, the ring electrode area was 0.1886 cm$^{-2}$, and the theoretical collection rate was 0.37. To prepare the working electrode, 5 mg of catalyst was dispersed in 500 uL of ethanol solution and 500 uL of deionized water, followed by adding 50 uL of Nafion binder. Subsequently the catalyst ink was prepared through ultrasonication, and 20 uL of ink was taken and dropped on RDE. After drying, a film was formed at room temperature. All catalysts were activated to stable CV in a saturated $N_2$ or $O_2$ electrolyte at a 40-turn scanning rate of 50 mV·s$^{-1}$, and the process CV curve was recorded. Linear sweep voltammetry (LSV) tests were performed in the voltage range of 0–0.8 V *vs.* RHE at a sweep rate of 50 mV·s$^{-1}$ under $O_2$ saturation conditions. The Koutecky–Levich (K–L) equation was then used to calculate the electron transfer number ($n$) during the ORR process based on obtained LSV date at various rotation rates of the RDE, which is expressed as follows:

$$\frac{1}{J} = \frac{1}{J_K} + \frac{1}{J_L} = \frac{1}{J_K} + \frac{1}{B\sqrt{\omega}} \quad \text{(S2)}$$

$$B = 0.2nFC_O D_O^{\frac{2}{3}} v^{-\frac{1}{6}} \quad \text{(S3)}$$

where $J$ is the measured current density of the working electrode, $\omega$ is the angular velocity of the rotating electrode, $J_K$ and $J_L$ are the kinetic and diffusion limiting current densities, respectively, $F$ is the Faraday constant (96485 C·mol$^{-1}$), $v$ ($1.0 \times 10^{-2}$ cm$^2$·s$^{-1}$) is the kinematic viscosity of the 0.1 mol·L$^{-1}$ KOH solution, and $D_O$ ($1.9 \times 10^{-5}$ cm$^2$·s$^{-1}$) and $C_O$ ($2.9 \times 10^{-4}$ mol·L$^{-1}$) are the diffusivity and solubility of oxygen in the 0.1 mol·L$^{-1}$ KOH solution, respectively.

## 4 Theoretical calculation details

Density functional theory (DFT) calculation was performed by DMol3 code as implemented in Materials Studio. The generalized gradient approximation of Perdew–Burke–Ernzerhof (GGA-PBE) function was used to treat all the energy changes. The core treatment was effective core potentials (ECP) and the basis set was DNP v4.4. The $k$-point was set as 3 × 3 × 1 and the thickness of the vacuum region was 15 Å. Based on TEM and XRD results, CoSe (101) and $Ti_3C_2$ with mutually

matched crystallographic dimensions were used to construct the model of the CoSe/$Ti_3C_2$ heterostructure. The OOH adsorption free energy on the obtained surfaces (101) was calculated according to Eq. (4) as follows:

$$\Delta E_{OOH} = E_{(surf+OOH)} - E_{surf} - E_{OOH} \quad \text{(S4)}$$

where $E_{surf}$ and $E_{OOH}$ were related to the energy of bare surface and that of the single OOH molecule, respectively, and $E_{(surf+OOH)}$ represented the energy of total system with one adsorbed H atom in each unit cell.

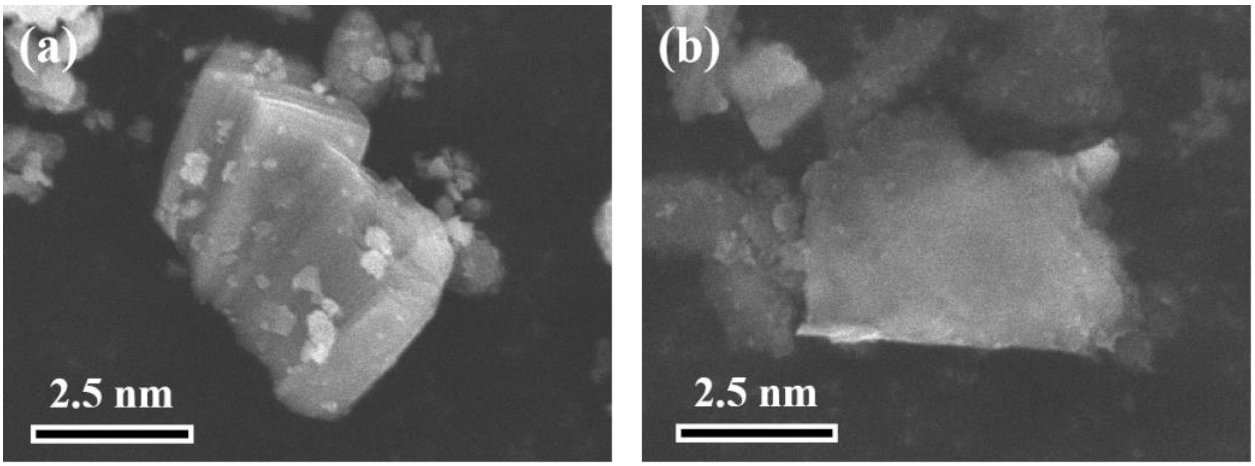


**Fig. S1** SEM images of **(a)** multi-layered $Ti_3C_2$ and **(b)** few-layered $Ti_3C_2$.

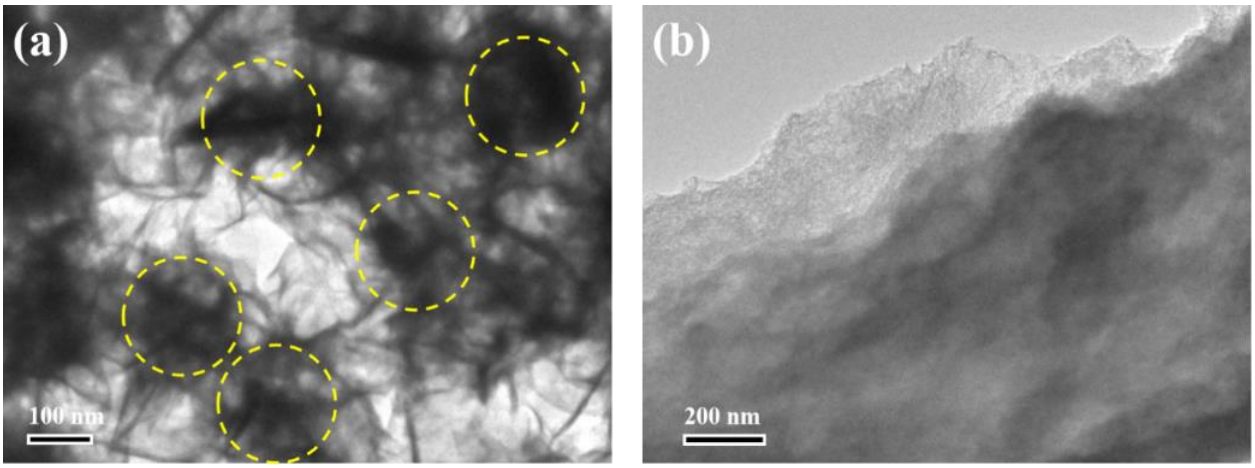


**Fig. S2** TEM images of **(a)** CoSe and **(b)** $Ti_3C_2$.

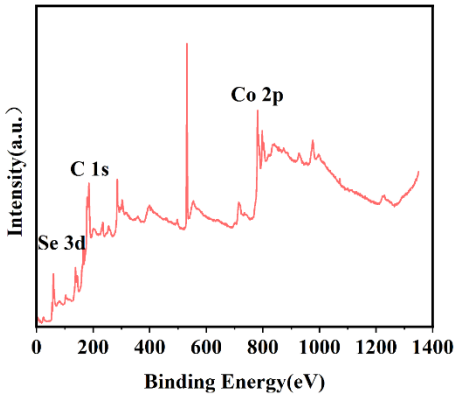


**Fig. S3** XPS survey spectrum of CoSe.

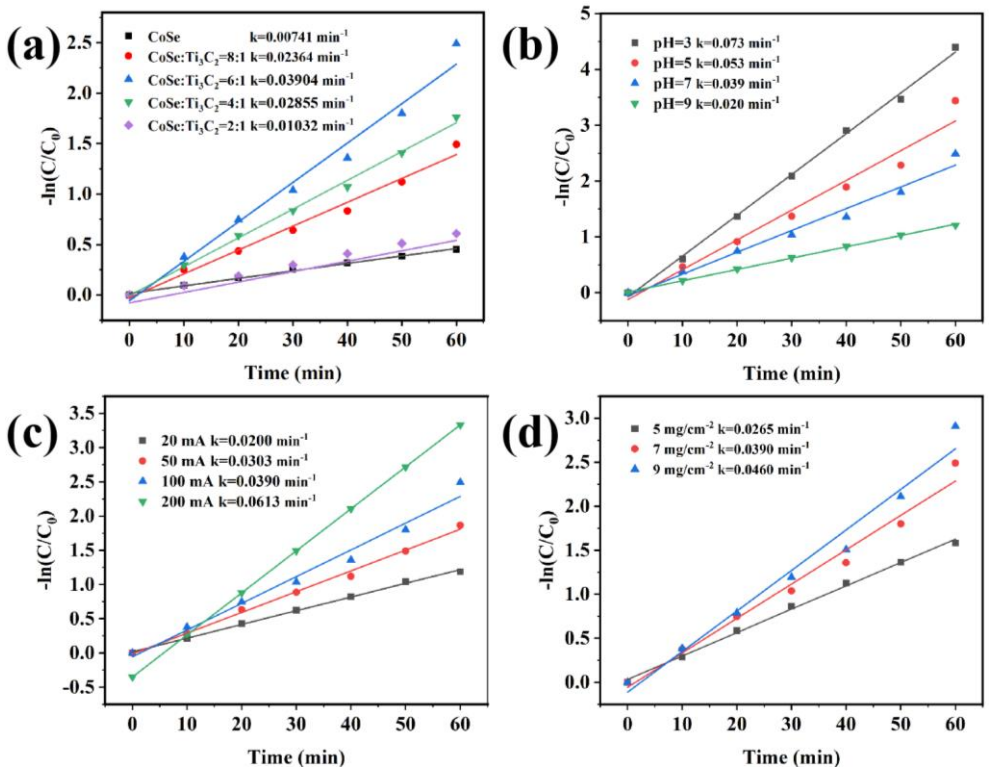


**Fig. S4** Determination of values of the reaction rate constant *k* according to **(a)** different ratios of CoSe to $Ti_3C_2$, **(b)** different pH values, **(c)** different currents, and **(d)** different catalyst loadings.

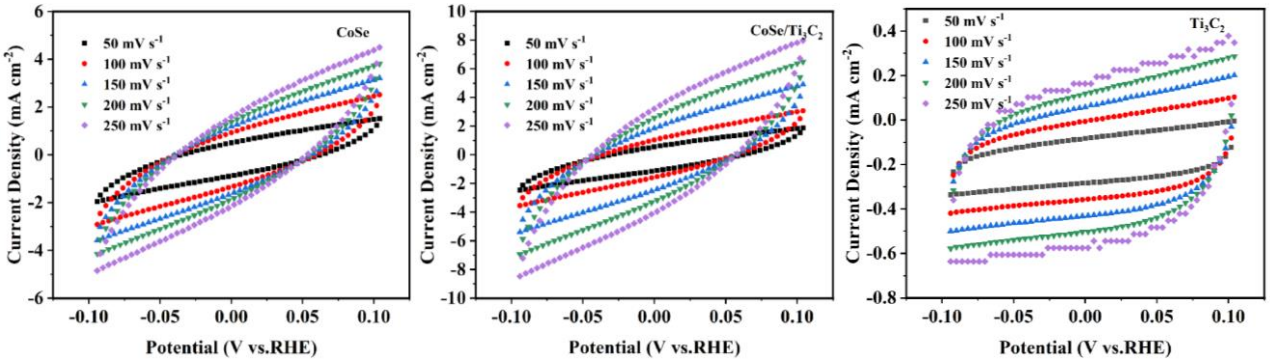


**(a)** **(b)** **(c)**

**Fig. S5** CV results for different samples in the region from −0.1 to 0.1 V *vs.* RHE at the scan rate ranging from 50 to 250 $mV \cdot s^{-1}$.

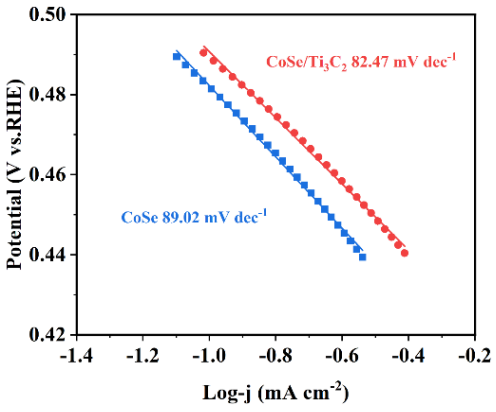


**Fig. S6** Determination of Tafel slopes for $CoSe/Ti_3C_2$ and CoSe.

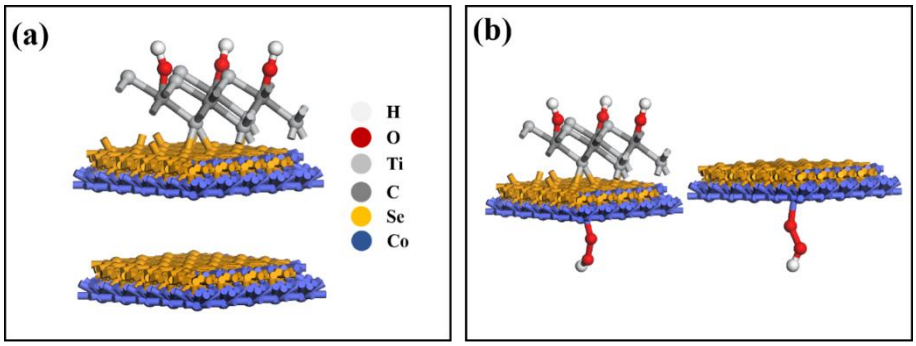


**Fig. S7 (a)** Structure models **(b)** *OOH adsorption models of both CoSe/$Ti_3C_2$ and CoSe.

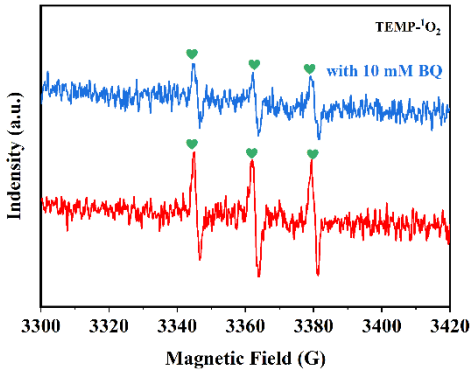


**Fig. S8** EPR spectra of TEMP-$^1O_2$. Conditions: 100 mA, pH = 7, *c*(BQ) = 10 mmol·$L^{-1}$.

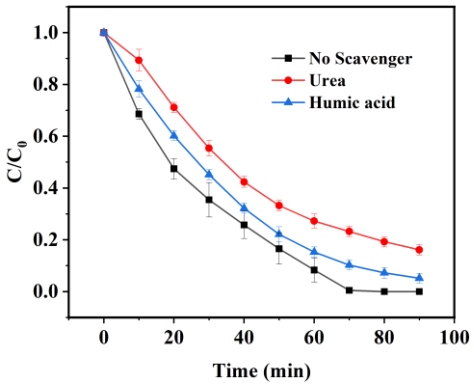


**Fig. S9** Comparison of degradation performance under different conditions: in the absence of scavengers; in the presence of 20 mmol·$L^{-1}$ urea; in the presence of 20 mmol·$L^{-1}$ humic acid.

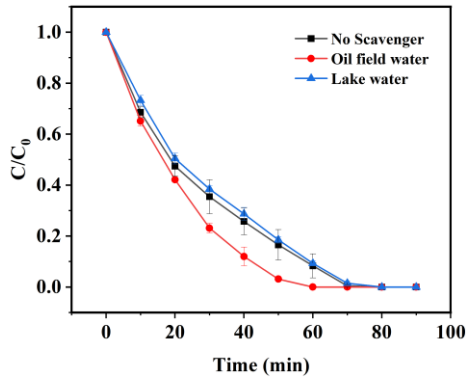


**Fig. S10** Comparison of degradation performance using different background water: without scavenger; with oil-field water; with lake water.

**Table S1** Comparison of performance between the catalyst in this work and other previously reported catalysts for the degradation of SMR

| Material | AOPs type | $c_p$/(mg·L$^{-1}$) [a] | $t$/min | $\eta$/% [b] | Experimental conditions | $k$/min$^{-1}$ | Ref. |
|---|---|---|---|---|---|---|---|
| $Fe_2O_3$–$CeO_2$ | Fenton-like | 20 | 75 | 100 | pH = 3.0, $c_{ct}$ = 0.5 g·L$^{-1}$ [c], $c_{hp}$ = 8 mmol·L$^{-1}$ [d], $T$ = 45 °C | 0.025 | [S1] |
| $FeS_2$NWs/$Ti_3C_2$ | Hetero-EF | 10 | 80 | 97.6 | 200 mA, pH = 3 | 0.046 | [S2] |
| $CoS_2$/CoS/$Ti_3C_2$ | Photoelectro -Fenton | 10 | 120 | 98.5 | 15 mA·cm$^{-2}$, pH=3 | 0.031 | [S3] |
| O- and F-doped porous carbon | Metal-free electro-Fenton | 20 | 180 | 90.1 | −1.5 V, pH = 3 | 0.012 | [S4] |
| CNO-30 | Photocatalysis | 10 | 240 | 72.64 | Visible light | 0.00507 | [S5] |
| La-$CeO_2$-5 | Photocatalysis | 10 | 240 | 81 | Visible light | – | [S6] |
| CoSe/$Ti_3C_2$ | Hetero-EF | 10 [e] | 80 | 100 | 100 mA, pH = 6.8 | 0.039 | This work |

a) $c_p$, the concentration of pollutant; b) $\eta$, the removal efficiency; c) $c_{ct}$, the concentration of catalyst; d) $c_{hp}$, the concentration of hydrogen peroxide, i.e., $c(H_2O_2)$; e) the concentration of sulfamerazine.

## References


[S1] Gao P, Chen X J, Hao M J, et al. Oxygen vacancy enhancing the $Fe_2O_3$–$CeO_2$ catalysts in Fenton-like reaction for the sulfamerazine degradation under $O_2$ atmosphere. Chemosphere, 2019, 228: 521–527

[S2] Xia Y, Yang F, Zhang B, et al. Fabrication of novel $FeS_2$ NWs/$Ti_3C_2$ cathode for photo-electro-Fenton degradation of sulfamethazine. Chemical Engineering Journal, 2021, 426: 130719

[S3] Chen F J, Yang F, Che S, et al. Titanium carbide composite hollow cobalt sulfide heterojunction with function of promoting electron migration for efficiency photo-assisted electro-Fenton cathode. Catalysts, 2023, 13(2): 253

[S4] Li Y, Cao W X, Zuo X J. O- and F-doped porous carbon bifunctional catalyst derived from polyvinylidene fluoride for sulfamerazine removal in the metal-free electro-Fenton process. Environmental Research, 2022, 212: 113508

[S5] Cao S H, Zhang Y, Ding K Q, et al. Efficient visible light driven degradation of antibiotic pollutants by oxygen-doped graphitic carbon nitride via the homogeneous supramolecular assembly of urea. Environmental Research, 2022, 210: 112920

[S6] Cao S H, Qu J R, Zhao Y Q, et al. Visible-light-driven photocatalysis degradation of antibiotic pollutants by La-doped $CeO_2$ nanorods: synergy of La doping and oxygen vacancy. Rare Metals, 2024, 43: 3134–3145